Monthly Notices
of the
ROYAL ASTRONOMICAL SOCIETY

Mon. Not. R. Astron. Soc. **418,** 2113–2120 (2011) doi:10.1111/j.1365-2966.2011.19232.x

Characterization of long baseline calibrators at 2.3 GHz

F. Hungwe,[1,2⋆] R. Ojha,[3,4⋆] R. S. Booth,[1,2] M. F. Bietenholz,[1,5] A. Collioud,[6,7] P. Charlot,[6,7] D. Boboltz[4] and A. L. Fey[4]

[1]*Department of Physics and Electronics, Rhodes University, PO Box 94, Grahamstown 6140, South Africa*
[2]*Hartebeesthoek Radio Astronomy Observatory, PO Box 443, Krugersdorp 1740, South Africa*
[3]*NVI, Inc., 7257D Hanover Parkway, Greenbelt, MD 20770, USA*
[4]*United States Naval Observatory, 3450 Massachusetts Ave., NW, Washington DC 20392, USA*
[5]*Department of Physics and Astronomy, York University, Toronto, ON M3J 1P3, Canada*
[6]*Observatoire Aquitain des Sciences de l'Univers, Université de Bordeaux, BP 89, 33271 Floirac Cedex, France*
[7]*CNRS, Laboratoire d'Astrophysique de Bordeaux-UMR 5804, BP 89, 33271 Floirac Cedex, France*

Accepted 2011 June 11. Received 2011 May 24; in original form 2010 October 29

ABSTRACT

We present a detailed multi-epoch analysis of 31 potential Southern hemisphere radio calibrators that were originally observed as part of a programme to maintain the International Celestial Reference Frame. At radio wavelengths, the primary calibrators are active galactic nuclei (AGNs), powerful radio emitters which exist at the centre of most galaxies. These are known to vary at all wavelengths at which they have been observed. By determining the amount of radio source structure and variability of these AGNs, we determine their suitability as phase calibrators for long baseline radio interferometry at 2.3 GHz. For this purpose, we have used a set of complementary metrics to classify these 31 southern sources into five categories pertaining to their suitability as very long baseline interferometry calibrators. We find that all of the sources in our sample would be good interferometric calibrators, and almost ninety per cent of them would be very good calibrators.

Key words: techniques: high angular resolution – techniques: interferometric – galaxies: active – galaxies: jets – quasars: general – radio continuum: galaxies.

1 INTRODUCTION

High angular resolution observations of weak radio sources (where self-calibration is not possible) require calibrator sources for correction of systematic effects and effects of the atmosphere on the measured visibilities. Atmospheric fluctuations cause perturbations in visibility phase which, if not corrected, seriously limit both the sensitivity and image quality of an interferometric array. Phase calibrators are also required for astrometric observations. An ideal calibrator would look the same on all observing baselines. It should be bright, unresolved or at least compact and should not vary. A calibrator source should also be separated from the target sources by as small an angle as possible in order to look along the same line of sight throughout the atmosphere. Therefore, it is desirable to have calibrator sources evenly distributed across the whole sky. In practice, at radio wavelengths, calibrators are mostly active galactic nuclei (AGNs), whose fundamental source of power is believed to be the accretion of matter on to a super-massive black hole (e.g. Rees 1997). They are known to vary at every wavelength at which they have been studied. AGNs are very compact and isotropically distributed around the sky. They are also very distant objects and therefore, generally, have no discernible proper motions on the sky. It is these qualities that make them suitable as calibrators at radio wavelengths.

Due to the limited number of radio telescopes, few surveys for calibrators have been carried out in the Southern hemisphere (Fey et al. 2004a,b, 2006; Ojha et al. 2004a, 2005). Hence, there are fewer known calibrators in the south. A major expansion of radio astronomy observing capability is underway in the Southern hemisphere. Two Square Kilometre Array (SKA) precursors, the South African Karoo Array Telescope (MeerKAT; Booth et al. 2009) and Australian SKA Pathfinder (ASKAP; Johnston et al. 2008) are presently under construction, leading to the SKA itself. It is clear that interferometry and very long baseline interferometry (VLBI) in the Southern hemisphere need a dense network of calibration sources at high resolutions and a range of frequencies. MeerKAT is the South African SKA demonstrator telescope. When completed, it will be the largest radio telescope array in the Southern hemisphere. It will operate in two frequency ranges: 0.58–2.5 and 8–14.5 GHZ (Booth et al. 2009). MeerKAT will participate in VLBI observations with the European VLBI network

⋆E-mail: faith@hartrao.ac.za (FH); roopesh.ojha@gmail.com (RO)

and other VLBI arrays. The SKA will operate in the frequency range 0.7–25 GHz (Carilli & Rawlings 2004; Schilizzi 2007) and is expected to have much longer baselines for which a southern VLBI calibrator list will be essential.

The United States Naval Observatory (USNO) in collaboration with National Aeronautics and Space Administration (NASA), the Laboratoire d'Astrophysique de Bordeaux (LAB) and the National Radio Astronomy Observatory (NRAO)[1] has since 1994 been observing AGNs, once every two months, through the research and development of VLBI (RDV) experiments. This has led to a wealth of data of sources observed simultaneously at 2.3 and 8.4 GHz at regular epochs. Images of these AGNs form the USNO's Radio Reference Frame Image Database (RRFID) and LAB's Bordeaux VLBI Image Database (BVID)[2] (Fey, Clegg & Fomalont 1996; Fey & Charlot 1997, 2000; Collioud & Charlot 2009). The RRFID is a data base of about 6700 images of over 700 AGN sources compiled from geodetic and astrometric VLBI experiments. The BVID contains over 1800 images of 824 radio sources. It is the goal of the ongoing RDV programme to image the radio reference frame sources on a regular basis to monitor them for variability and structural change. Piner et al. (2007) discuss jet kinematics in a subset of the RRFID sources, concentrating on the 8.4 GHz observations. Their survey is made up of RRFID sources that have been observed at three or more epochs from 1994 July to 1998 December.

In this paper, we focus on 2.3 GHz observations of a sample of 31 potential southern VLBI calibrators (with declinations between 0° and -60°) from the kinematic survey of Piner et al. (2007). The choice of 2.3 GHz was made because both MeerKAT and ASKAP will be operating at frequencies close to this. We seek to characterize this selection of southern radio sources and determine their suitability as calibrators for southern VLBI experiments, especially those using MeerKAT and the SKA when completed.

In the following sections, we will describe the observations and data reduction process. We will then describe the imaging and model-fitting process and go on to analyse the data and discuss the results.

2 OBSERVATIONS AND DATA REDUCTION

RDV experiments are carried out using the 10 antennas of the NRAO's Very Long Baseline Array (VLBA) and up to 10 other antennas across the globe, including Hartebeesthoek (South Africa) when available. The use of the global array greatly improves the $u-v$ coverage. Hartebeesthoek greatly improves the $u-v$ coverage for sources in the south, which make up the sample in this paper.

The 31 southern sources included in our sample are listed in Table 1 along with their optical properties. The source sky distribution is shown in Fig. 1. The RDV observing epochs are from 1994 July to 2008 January, giving a total of 32 epochs and an average of 20 epochs per source. About 100 sources were observed in each 24 h observing run, with an average on-source time of 15 min. The on-source time is not continuous, but divided into scans of between one and several minutes long, spaced in time to give optimal $u-v$ coverage.

[1] The National Radio Astronomy Observatory is a facility of the National Science Foundation operated under cooperative agreement by Associated Universities, Inc.

[2] The web site for the RRFID is located at http://rorf.usno.navy.mil/rrfid.shtml and the BVID at http://www.obs.u-bordeaux1.fr/BVID/

Observations were made in a dual frequency bandwidth synthesis mode to facilitate delay measurements for astrometry. Observations in this mode also allow imaging at both frequency bands. Eight individual frequency bands (IFs) were recorded simultaneously, each 8 MHz wide, with four at 2.3 GHz and four at 8.4 GHz for a total of 32 MHz in each frequency band.

The data were correlated with the VLBA correlator at the Array Operations Center in Socorro, New Mexico. The correlated data were calibrated and corrected for time- and frequency-dependent phase variations using NRAO's Astronomical Imaging Processing System (AIPS; Greisen 1998). Initial amplitude calibration for each IF was accomplished using system temperature measurements and gain curves generated during observations. Fringe fitting was done in AIPS using a solution interval equal to the scan duration and a point-source model.

Amplitude calibration was improved in the second stage by using observations of sources whose core flux density is known to be $\geq$90 per cent of the total flux density. For a precise definition of the core, refer to Section 3.1. To this end, a single amplitude gain correction factor was derived for each antenna based on fitting a Gaussian model to the core component. Gain correction factors were then calculated based on the difference between the observed and the model visibilities. Finally, the amplitude gain correction factors were applied to the target sources. This is a non-standard procedure that improves the overall amplitude calibration. The accuracy of the amplitude calibration determined in this way is conservatively estimated to be within 20 per cent.

Data imaging and model fitting were done using the CALTECH difference mapping program 'DIFMAP' (Shepherd, Pearson & Taylor 1995), after inspecting the data and editing out obvious bad points. The data were imaged using DIFMAP in the automatic mode. Generally, this mode fails for about one-third of the sources which have a structure that is complex or too extended for the automatic script to handle. These have to be redone by hand in an interactive mode. For the southern sources in this sample, almost all had to be imaged by hand due to the poor $u-v$ coverage.

DIFMAP combines the visibilities in all four 2.3 GHz receiver IFs but does not correct for spectral index effects. It was assumed that the source structure variations across the IFs were negligible (6 per cent variation in frequency at this band). Uniform weighting was used for the initial phase self-calibration before changing to natural weighting. For our arrays, uniform weighting gives more weighting to the longer baselines, whilst natural weighting gives more weighting to the shorter baselines. Images of six of the 31 sources in our sample are shown in Fig. 2 with the remainder available online (see supporting information). Images of additional epochs can be found in the form of contour plots at the RRFID and BVID websites.

Generally, circular Gaussian models were used to fit the $u-v$ data in order to parametrize the source morphology. Like imaging, model fitting is an iterative process. Elliptical Gaussian components were used only to represent the core component or a very bright jet component if the residuals remaining from a circular Gaussian model were too large and made it difficult to continue model fitting using the residual map. The model fits generally describe the visibility of data well, but these models may not be unique because of incomplete sampling in the $u-v$ plane. In order to determine the suitability of a source as a calibrator, we then determine the amount of source structure, as well as its variation with time, using several different methods based on both the CLEAN components from the DIFMAP imaging and on the parameters of the fitted Gaussians.

Table 1. Optical and radio properties of the sample. The positions shown above are the most recent International Celestial Reference Frame positions (Fey, Gordon & Jacobs 2009). $S_{\rm core}$ is the flux density in the Gaussian component fitted to the core of the latest epoch, while the total flux density $S_{\rm total}$ is the sum of the CLEAN COMPONENTS.

B1950 Source name	Other name	Optical ID	z	Co-ordinates RA (hh mm ss)	Dec. (deg mm ss)	Latest flux densities $S_{\rm total}$	$S_{\rm core}$	Latest epoch
0003−066		BL Lac	0.35[a]	00 06 13.892 888 49	−06 23 35.335 3162	2.29	1.79	2008 Jan
0104−408		BL Lac	0.58[b]	01 06 45.107 968 51	−40 34 19.960 2291	1.51	1.52	2008 Jan
0238−084	NGC1052	Galaxy	0.005[c]	02 41 04.798 502 56	−08 15 20.751 7956	0.53	0.26	2007 Dec
0336−019	CTA26	Quasar	0.85[d]	03 39 30.937 787 51	−01 46 35.804 1062	2.53	2.16	2008 Jan
0402−362		Quasar	1.42[e]	04 03 53.749 898 35	−36 05 01.913 1085	0.91	0.99	2007 Mar
0454−234		Quasar	1.00[a]	04 57 03.179 228 63	−23 24 52.020 1418	3.41	3.01	2007 Dec
0458−020		Quasar	2.29[f]	05 01 12.809 883 66	−01 59 14.256 2534	0.82	0.65	2007 Dec
0727−115		Quasar	1.59[g]	07 30 19.112 474 20	−11 41 12.600 5110	3.77	3.47	2008 Jan
0919−260		Quasar	2.30[h]	09 21 29.353 855 35	−26 18 43.386 1684	1.58	1.50	2006 Sep
0920−397		Quasar	0.59[i]	09 22 46.418 260 64	−39 59 35.068 3561	1.56	1.49	2008 Jan
1034−293		Quasar	0.31[a]	10 37 16.079 734 76	−29 34 02.813 3345	1.60	1.51	2008 Jan
1124−186		Quasar	1.05[j]	11 27 04.392 449 58	−18 57 17.441 6582	1.16	1.16	2008 Jan
1144−379		Quasar	1.05[a]	11 47 01.370 701 77	−38 12 11.023 4199	1.09	1.09	2007 Jan
1145−071		Quasar	1.34[k]	11 47 51.554 028 76	−07 24 41.141 0887	0.95	0.81	2007 Jan
1253−055	3C279	Quasar	0.54[l]	12 56 11.166 565 41	−05 47 21.524 7030	7.60	7.30	1998 Dec
1255−316		Quasar	1.92[m]	12 57 59.060 817 37	−31 55 16.851 6980	1.51	1.38	2008 Jan
1313−333		Quasar	1.21[n]	13 16 07.985 939 95	−33 38 59.172 5057	0.76	0.53	2004 Feb
1334−127		Quasar	0.54[o]	13 37 39.782 777 68	−12 57 24.693 2620	2.61	2.57	2008 Jan
1351−018		Quasar	3.71[p]	13 54 06.895 322 13	−02 06 03.190 4447	1.00	0.98	2008 Jan
1424−418		Quasar	1.52[b]	14 27 56.297 565 36	−42 06 19.437 5991	2.04	1.66	2008 Jan
1451−375		Quasar	0.31[q]	14 54 27.409 754 42	−37 47 33.144 8724	0.56	0.51	2006 Jul
1514−241		BL Lac	0.05[r]	15 17 41.813 132 21	−24 22 19.476 0251	2.94	2.24	2007 Jan
1622−253		Quasar	0.79[s]	16 25 46.891 640 10	−25 27 38.326 7989	1.01	0.99	2008 Jan
1741−038		Quasar	1.05[b]	17 43 58.856 133 96	−03 50 04.616 6450	4.78	4.73	2008 Jan
1908−201		Quasar	1.12[t]	19 11 09.652 891 98	−20 06 55.108 9891	2.10	1.78	2007 Dec
1921−293		Quasar	0.35[i]	19 24 51.055 955 14	−29 14 30.121 0524	6.18	5.43	2007 Dec
1954−388		Quasar	0.63[u]	19 57 59.819 274 70	−38 45 06.355 7585	2.75	2.69	2008 Jan
1958−179		Quasar	0.65[u]	20 00 57.090 444 85	−17 48 57.672 5440	1.53	1.56	2007 Dec
2052−474		Quasar	1.49[m]	20 56 16.359 818 74	−47 14 47.627 6461	1.37	1.43	2007 Dec
2243−123		Quasar	0.63[u]	22 46 18.231 976 13	−12 06 51.277 4796	2.57	1.33	2008 Jan
2255−282		Quasar	0.93[e]	22 58 05.962 884 81	−27 58 21.256 7425	0.95	0.87	2008 Jan

[a]Stickel, Fried & Kuehr (1989); [b]White et al. (1988); [c]Denicoló et al. (2005); [d]Wills et al. (1978); [e]Peterson et al. (1976); [f]Strittmatter et al. (1974); [g]Zensus et al. (2002); [h]Wright et al. (1979); [i]Hewitt & Burbidge (1989); [j]Linfield et al. (1989); [k]Wilkes et al. (1986); [l]Marziani et al. (1996); [m]Jauncey et al. (1984); [n]Jauncey et al. (1982); [o]Stickel, Kuehr & Fried (1993); [p]Osmer, Porter & Green (1994); [q]Jones et al. (2004); [r]Jones et al. (2009); [s]di Serego-Alighieri et al. (1994); [t]Halpern, Eracleous & Mattox (2003); [u]Browne, Savage & Bolton (1975).

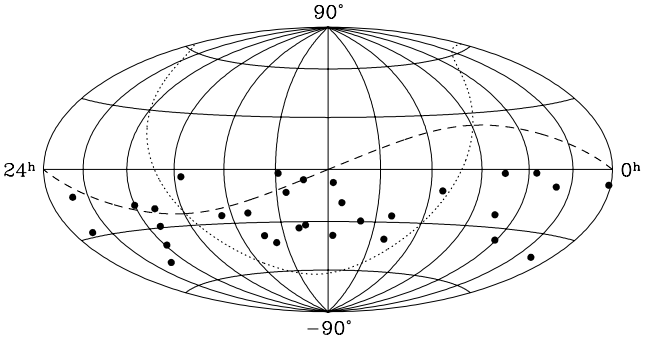

Figure 1. Sky distribution of the southern sources plotted on an Aitoff equal-area projection of the celestial sphere. The dotted line represents the Galactic plane, while the dashed line is the ecliptic.

3 ANALYSIS AND RESULTS

Characterization of the morphology of an AGN is very complex, and no single metric is able to adequately define a good calibrator. Thus, we have developed a number of complementary approaches that are described below. A weighted combination of all of these metrics is eventually used to classify the suitability of each source to be a high-resolution phase calibrator. These are discussed in the following sections.

3.1 Core flux density

A good calibrator should be relatively bright at the frequency of observation to be easily detectable. It should also be stable with minimal flux density variation over time. There is no precise definition of the AGN 'core' in the literature. In general, the bright, compact flat spectrum feature is referred to as the core. We have confirmed our identification of the cores for our entire sample by establishing that these structures have flat or inverted spectra. This was done by using the 8.4 GHz data that are observed simultaneously with the 2.3 GHz observations presented here. Here, we define a core flux density, $S_{\rm core}$, for each source and for each epoch as the flux density of the Gaussian component fitted to the core. The latest core flux density as defined in this section is shown for each source in Table 1. From the core flux density, we computed the mean core flux density ($\bar{S}$) averaged over all epochs in which the source was

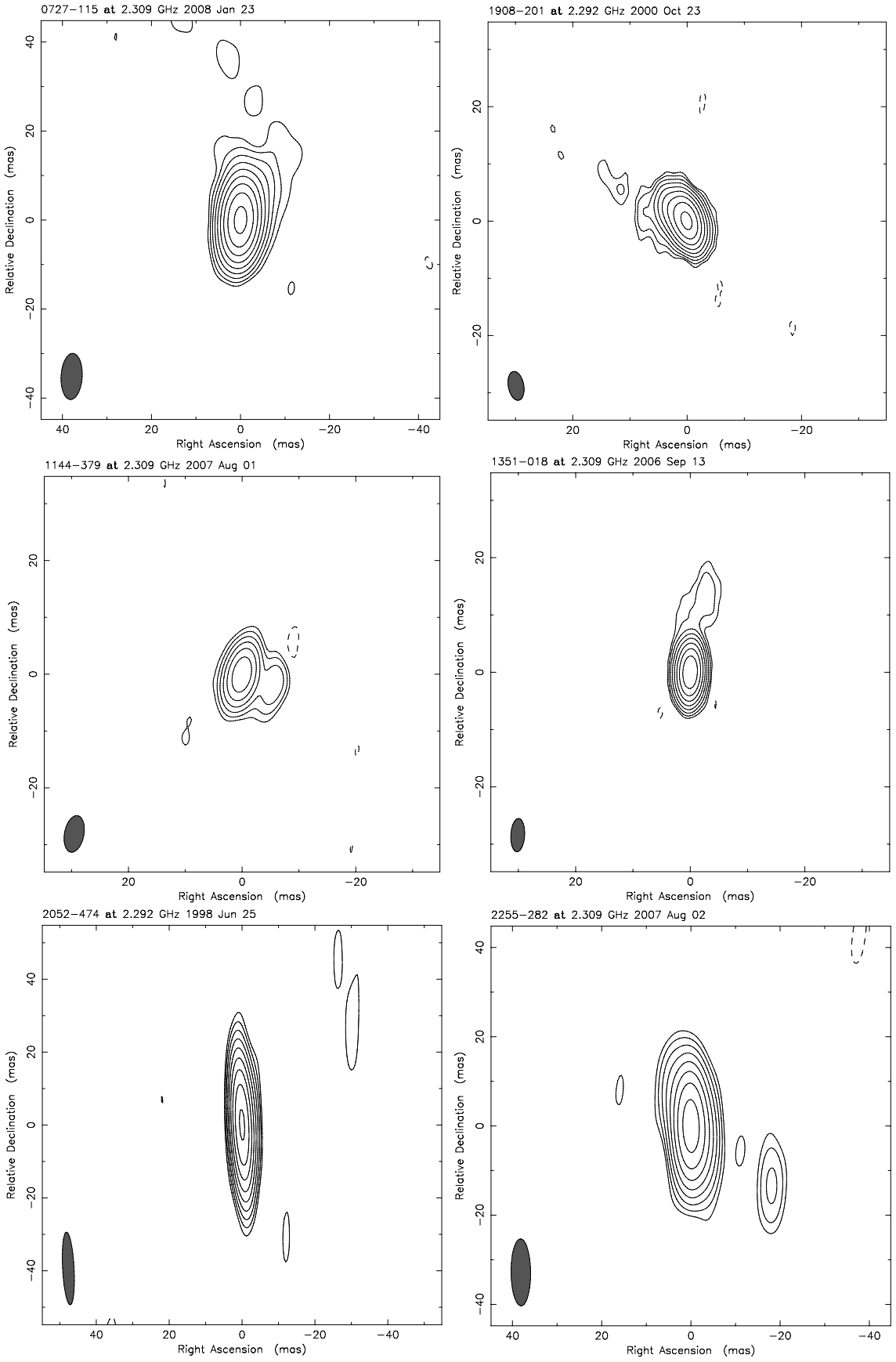

Figure 2. Two examples each of class 'A', 'B' and 'C' sources, respectively. Our current sample contains no examples of classes 'D' and 'E'.

Table 2. Results of variability analysis in the flux density, core fraction and radial extent.

Source name	Epochs	Core flux density			Core fraction			Weighted radial extent			Unweighted radial extent		
		$\bar{S}$	$\sigma_{\rm core}$	$\sigma_{\rm core}/\bar{S}$	$\bar{C}$	$\sigma_{\rm C}$	$\sigma_{\rm C}/\bar{C}$	$\bar{R}_{\rm W}$	$\sigma_{R_{\rm W}}$	$\sigma_{R_{\rm W}}/\bar{R}_{\rm W}$	$\bar{R}_{\rm UW}$	$\sigma_{R_{\rm UW}}$	$\sigma_{R_{\rm UW}}/\bar{R}_{\rm UW}$
0003−066	24	1.55	0.31	0.20	0.64	0.07	0.11	1.67	0.40	0.24	6.17	2.22	0.36
0104−408	28	1.26	0.29	0.23	1.00	0.04	0.04	0.93	1.24	1.33	7.86	17.13	2.18
0238−084	16	0.91	0.20	0.22	0.53	0.10	0.19	0.37	0.10	0.27	17.34	16.13	0.93
0336−019	25	1.92	0.48	0.25	0.80	0.08	0.10	1.00	0.64	0.64	3.05	2.32	0.76
0402−362	17	1.22	0.11	0.09	1.00	0.03	0.03	1.18	0.26	0.22	8.11	4.54	0.56
0454−234	27	1.73	0.59	0.34	1.00	0.02	0.02	0.46	0.31	0.67	3.18	1.78	0.56
0458−020	26	0.78	0.31	0.40	0.68	0.15	0.22	2.22	1.02	0.46	16.30	17.93	1.10
0727−115	32	2.37	0.71	0.30	0.83	0.05	0.06	1.15	0.30	0.26	6.10	1.77	0.29
0919−260	17	1.32	0.83	0.63	0.73	0.11	0.15	1.70	0.34	0.20	6.46	1.55	0.24
0920−397	16	1.06	0.18	0.17	0.92	0.11	0.12	1.81	0.94	0.52	7.27	2.98	0.41
1034−293	27	1.11	0.30	0.27	0.88	0.21	0.24	0.91	0.68	0.75	5.83	8.22	1.41
1124−186	26	0.90	0.19	0.21	1.00	0.02	0.02	0.25	0.29	1.18	6.88	16.50	2.40
1144−379	23	1.34	0.39	0.29	0.83	0.05	0.06	0.44	1.79	4.10	9.61	20.66	2.15
1145−071	16	0.69	0.11	0.16	0.77	0.10	0.13	1.33	0.24	0.18	6.11	2.26	0.37
1253−055	3	6.75	0.27	0.04	0.65	0.15	0.23	2.27	0.25	0.11	12.5	0.50	0.04
1255−316	14	1.20	0.24	0.20	0.79	0.11	0.14	2.68	0.67	0.25	14.12	11.86	0.84
1313−333	17	0.80	0.28	0.35	0.71	0.05	0.07	1.29	0.40	0.31	7.82	3.05	0.39
1334−127	25	2.12	0.55	0.26	1.00	0.04	0.04	0.84	0.62	0.74	3.60	1.87	0.52
1351−018	13	0.78	0.25	0.32	1.00	0.03	0.03	1.51	2.93	1.94	2.55	1.86	0.73
1424−418	18	1.69	0.49	0.29	0.73	0.08	0.11	3.42	1.88	0.55	22.55	11.07	0.47
1451−375	14	1.11	0.30	0.27	0.88	0.07	0.08	0.37	3.71	10.08	9.31	5.40	0.58
1514−241	16	1.76	0.30	0.17	0.83	0.05	0.06	3.39	0.78	0.23	18.57	3.90	0.21
1622−253	24	1.27	0.38	0.30	0.83	0.05	0.06	1.26	0.72	0.57	6.35	7.37	1.16
1741−038	28	3.18	1.05	0.33	1.00	0.03	0.03	0.33	0.22	0.66	2.17	1.24	0.57
1908−201	23	1.95	0.45	0.23	0.77	0.07	0.09	1.50	0.45	0.30	5.60	1.68	0.30
1921−293	23	7.42	2.45	0.33	0.60	0.09	0.15	2.30	0.53	0.23	8.78	8.17	0.93
1954−388	21	2.16	0.54	0.25	1.00	0.05	0.05	0.56	0.52	0.93	3.52	2.71	0.77
1958−179	9	1.16	0.52	0.45	0.80	0.04	0.05	0.17	0.56	3.29	2.79	2.29	0.82
2052−474	10	1.36	0.34	0.25	0.81	0.29	0.36	1.33	2.09	1.56	10.45	10.66	1.02
2243−123	22	1.50	0.33	0.22	0.86	0.06	0.07	2.00	0.48	0.24	9.32	1.77	0.19
2255−282	20	0.95	1.11	1.17	0.77	0.10	0.13	2.30	2.05	0.89	6.58	3.49	0.53

observed. The extent to which the core flux density varies over time can be characterized by the variability index ($\sigma_{\rm core}/\bar{S}$) of the core flux density, where $\sigma_{\rm core}$ is the standard deviation of the core flux density. A value of 0.0 indicates no variation over time (Table 2, Column 5).

Fig. 3 shows that 90 per cent of the sources have a variability index of the core flux density below 0.4 and 23 per cent of the sources have a variability index below 0.2 (which is below our estimated calibration uncertainties). These low variability indices indicate that most of the core fluxes in this sample are stable.

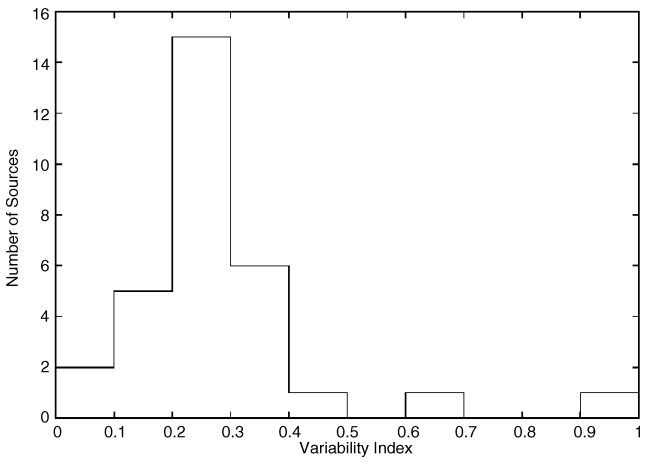

Figure 3. Distribution of the core flux density variability index.

3.2 Core fraction

Following Ojha et al. (2004b), we define a core fraction as

$$C = S_{\rm core\_cc}/S_{\rm total}, \quad (1)$$

where $S_{\rm core\_cc}$ is the sum of the flux densities of CLEAN components within one synthesized beam of the brightest pixel and $S_{\rm total}$ is the sum of all the CLEAN component flux densities.

It provides an indication of how point-like a source is and also provides a way to track source structure changes from epoch to epoch. The average core fraction, $\bar{C}$, was computed for each source over all epochs. As with the variability index of the core flux density, we also computed the variability index ($\sigma_{\rm C}/\bar{C}$) of the source core fraction, where $\sigma_{\rm C}$ is the standard deviation of the core fraction. A value of 0.0 for the variability index of the source core fraction indicates no variation over time. The results are shown in Table 2, Column 8.

The distribution of the variability index of the core fraction is shown in Fig. 4, while the distribution of the core fraction is shown in Fig. 5. The mean core fraction for all the sources is 83 per cent with a standard deviation of 12 per cent. All sources have a mean core fraction with the variability index below 0.4. 27 sources have a variability index between 0 and 0.2 and the remaining four between 0.21 and 0.4. In general, the southern sample sources are very

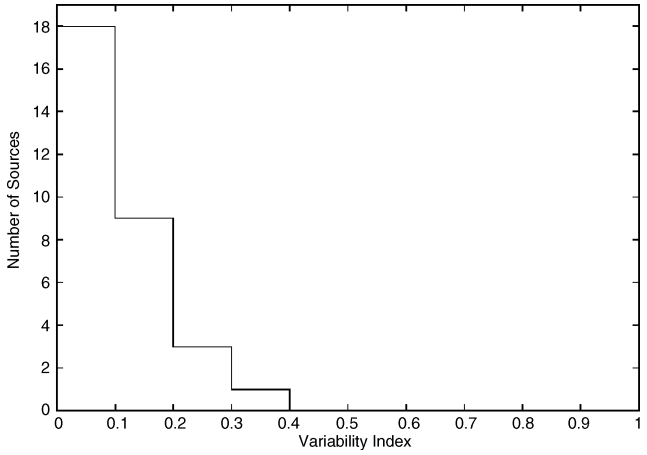

Figure 4. Distribution of the variability index of the core fraction. Note that all sources have a variablity index $\leq$0.4.

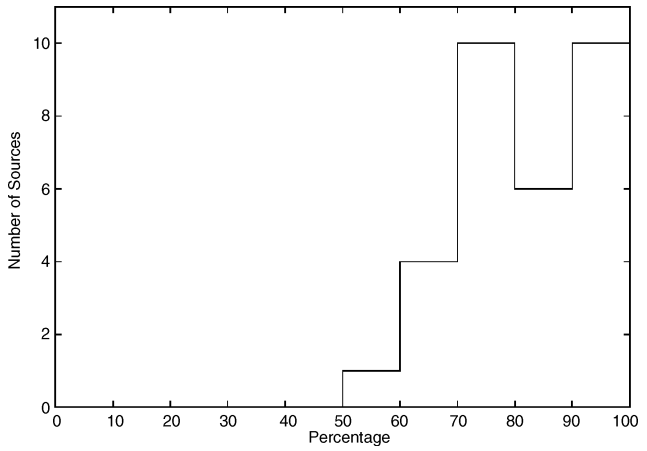

Figure 5. Distribution of the core fraction. This measure was used instead of the variability index as it shows slightly higher variation than the core fraction variability index.

compact with little variation. For this reason, we used the actual core fraction and not the variability index to classify the sources.

3.3 Flux-weighted radial extent

The previous two metrics are primarily measures of core-dominance. This and the following metric provide complementary information by quantifying the radial extent of the sources in the Southern sample.

The flux-density-weighted radial extent (Ojha et al. 2004b) is defined as

$$R_{\rm W} = \frac{\sum_i S_i r_i}{\sum_i S_i}, \quad (2)$$

where $R_{\rm W}$ is in units of milliarcseconds and r_i is the radius at which the ith CLEAN component has the flux density S_i.

The mean ($\bar{R}_{\rm W}$) and standard deviation were also calculated as was the variability index ($\sigma_{R_{\rm W}}/\bar{R}_{\rm W}$), where $\sigma_{R_{\rm W}}$ is the standard deviation of the weighted radial extent, see Table 2, Column 11.

The variability index of the weighted radial extent is widely distributed as shown in Fig. 6, with 10 per cent of the sources having an index between 0 and 0.2, showing minimal variation in the weighted radial extent. 32 per cent of the sources have an index between 0.21 and 0.40, while 13 per cent have an index between 0.41 and 0.60. 16 per cent of the sources have an index between 0.61 and 0.80, while the rest (29 per cent) have an index greater than 0.81. This shows a high degree of variability in the weighted radial extent.

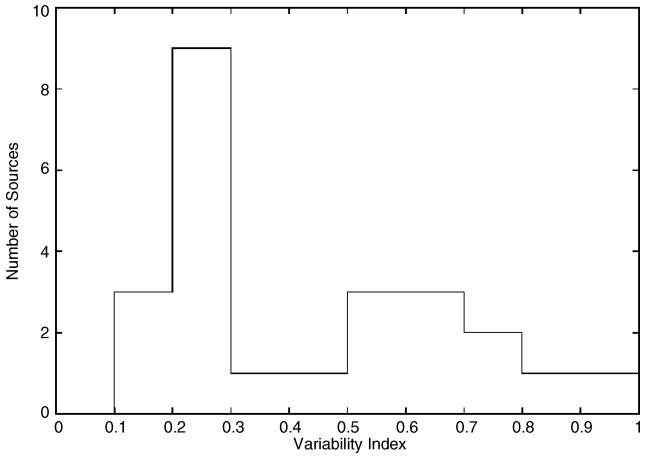

Figure 6. Distribution of the variability index of the weighted radial extent. Seven sources with the variability index greater than 1 are not shown in the histogram.

3.4 Unweighted radial extent

This is the radial extent within which 95 per cent of the flux density of the source is contained. This provides a measure of how extended a source is. The mean ($\bar{R}_{\rm UW}$) and standard deviations were calculated as was the variability index ($\sigma_{R_{\rm UW}}/\bar{R}_{\rm UW}$), where $\sigma_{R_{\rm UW}}$ is the standard deviation of the unweighted radial extent and $R_{\rm UW}$ is in units of milliarcseconds (Table 2, Column 14).

Like the variability index of the weighted radial extent (see above), the variability index of the unweighted radial extent is also widely distributed. Fig. 7 shows that 6 per cent of the sources have an index below 0.2, 23 per cent have an index between 0.21 and 0.40, while 29 per cent have an index between 0.41 and 0.60. About 10 per cent have an index between 0.61 and 0.80, while 35 per cent have an index greater than 0.80, showing very high variability in the unweighted radial extent. As discussed below, this high variability (in both the weighted and unweighted radial extents) is largely a

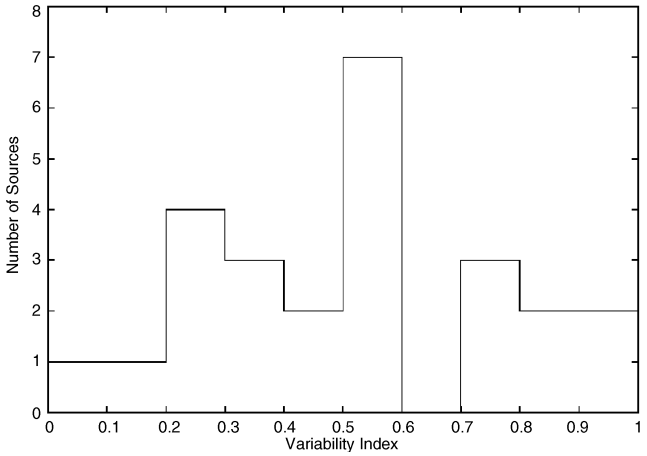

Figure 7. Distribution of the variability index of the unweighted radial extent. Six sources with the variability index greater than 1 are not shown in the histogram.

result of low brightness 'jet' features that are detected in some epochs but not others, usually due to differing sensitivities of the observing array rather than a real variation in the source.

4 SOURCE CLASSIFICATION

To capture the complexity of determining whether a radio source is a suitable phase calibrator for a radio interferometer, we have developed the set of complementary metrics described above. Here, we discuss how we combine the information these metrics provide to arrive at a classification scheme for potential calibrators. We explain our reasons for weighting the different metrics as we have done and present our recommendations based on this weighting scheme. Since such a scheme is necessarily somewhat subjective, it should be considered as reasonable and useful rather than a definitive classification.

The four metrics we used to classify the calibrator source quality were core fraction, core flux density variability index, weighted and unweighted radial extents. Each of these metrics is first assigned a score, with the scores as shown in Tables 3 and 4. The scores for the individual metrics were chosen so as to sum to 100 for a perfect calibrator source. We also chose to score the core fraction and core flux density variability so as to give them higher weight, each having a maximum score of 35, while the two radial extents have the maximum score of 15. We use a lower maximum score for the radial extents as they are highly sensitive to small epoch-to-epoch variations in the signal-to-noise ratio of the images. Faint extended features may be detected only at some epochs depending on the signal-to-noise ratio, resulting in a large variation in the radial-extent measures. Such low surface brightness features generally have negligible impact on the usefulness of the source as a calibrator. In any case, for a lower resolution array like MeerKAT these extended structures will be embedded in the main central component.

Based on the overall score summed up from this weighting scheme each source falls into one of the five classes 'A' through 'E'. A source falls into class 'A' if its overall score is between 80 and 100 per cent, class 'B' if the score is between 60 and 80 per cent, class 'C' if it scores between 40 and 60 per cent, class 'D' for any score between 20 and 40 per cent and class 'E' for sources scoring between 0 and 20 per cent. We propose the following classifications.

A – excellent calibrator (score between 80 and 100).
B – very good calibrator (score between 60 and 80).
C – good calibrator (score between 40 and 60).
D – use with caution (score between 20 and 40).
E – unsuitable as a calibrator (score below 20).

In our sample (Table 5), we have nine class 'A' sources, 19 class 'B' sources and three class 'C' sources. There are no sources in classes 'D' and 'E'. Thus, all the sources in our sample would be 'good' calibrators and all but three sources are likely to be 'very good' calibrators.

Table 3. Score distributions of the variability indices of the source core fraction and core flux density.

Core flux density variability index (per cent)	Score	Core fraction variability index	Score
>1	0.00		
0.91–1.00	3.5	91–100	35.0
0.81–0.90	7.0	81–90	31.5
0.71–0.80	10.5	71–80	28.0
0.61–0.70	14.0	61–70	24.5
0.51–0.60	17.5	51–60	21.0
0.41–0.50	21.0	41–50	17.5
0.31–0.40	24.5	31–40	14.0
0.21–0.30	28.0	21–30	10.5
0.11–0.20	31.5	11–20	7.0
0.01–0.10	35	1–10	3.5

Table 4. Distribution of scores for the variability index of the weighted and unweighted radial extents.

Index	Score
>1	0.00
0.91–1.00	1.5
0.81–0.90	3.0
0.71–0.80	4.5
0.61–0.70	6.0
0.51–0.60	7.5
0.41–0.50	9.0
0.31–0.40	10.5
0.21–0.30	12.0
0.11–0.20	13.5
0.01–0.10	15

Table 5. Classification of the sources. W_1: core flux density; W_2: core fraction; W_3: unweighted radial extent; W_4: weighted radial extent.

Source name	Score W_1	W_2	W_3	W_4	Total score (per cent)	Class
0003−066	31.5	31.5	10.5	12.0	85.5	A
0104−408	28.0	35.0	0.0	0.0	63.0	B
0238−084	28.0	31.5	1.5	12.0	73.0	B
0336−019	28.0	35.0	4.5	6.0	73.5	B
0402−362	35.0	35.0	7.5	12.0	89.5	A
0454−234	24.5	35.0	7.5	6.0	73.0	B
0458−020	24.5	31.5	0.0	9.0	65.0	B
0727−115	28.0	35.0	12.0	12.0	87.0	A
0919−260	14.0	31.5	12.0	13.5	71.0	B
0920−397	31.5	31.5	9.0	7.5	79.5	B
1034−293	28.0	28.0	0.0	4.5	60.5	B
1124−186	28.0	35.0	0.0	0.0	63.0	B
1144−379	28.0	35.0	0.0	0.0	63.0	B
1145−071	31.5	31.5	10.5	13.5	87.0	A
1253−055	35.0	28.0	15.0	13.5	91.5	A
1255−316	31.5	31.5	3.0	12.0	78.0	B
1313−333	24.5	35.0	10.5	10.5	80.5	A
1334−127	28.0	35.0	7.5	4.5	75.0	B
1351−018	24.5	35.0	4.5	0.0	64.0	B
1424−418	28.0	31.5	9.0	7.5	76.0	B
1451−375	28.0	35.0	7.5	0.0	70.5	B
1514−241	31.5	35.0	12.0	12.0	90.5	A
1622−253	28.0	35.0	0.0	7.5	70.5	B
1741−038	24.5	35.0	7.5	6.0	73.0	B
1908−201	28.0	35.0	12.0	12.0	87.0	A
1921−293	24.5	31.5	1.5	12.0	69.5	B
1954−388	28.0	35.0	4.5	1.5	69.0	B
1958−179	21.0	35.0	3.0	0.0	59.0	C
2052−474	28.0	24.5	0.0	0.0	52.5	C
2243−123	28.0	35.0	13.5	12.0	88.5	A
2255−282	00.0	31.5	7.5	3.0	42.0	C

5 CONCLUSIONS

We model fitted up to 32 epochs of observations (average of 20 epochs) for each of the 31 sources in our sample which was selected from the RRFID kinematic survey (Piner et al. 2007) and determined their suitability as phase calibrators. While the kinematic survey looks more at proper motion in the sources at 8.4 GHz, this paper concentrates on the morphological properties of the sources at 2.3 GHz, a frequency more relevant to emerging Southern hemisphere arrays like MeerKAT and ASKAP.

We have developed a method to classify radio sources according to their suitability as phase calibrators for radio interferometers. We first characterize a source by calculating several metrics which give measures of the degree to which the core dominates the source, and the degree of variability, both in flux density and the degree to which the source is extended. These metrics are then combined to give the source a total score, which is used to assign the source to one of the five classes of suitability as a calibrator. All 31 sources in our sample were classified as 'good' calibrators with 28 classified as 'very good' or better.

ACKNOWLEDGMENTS

FH is supported by a grant from the South African SKA project and HartRAO. FH thanks the USNO for their hospitality during her visits in 2008 and 2010. This research has made use of the USNO RRFID and LAB BVID. This research has made use of NASA's Astrophysics Data System Bibliographic Services and the NASA/IPAC Extragalactic Data base (NED), which is operated by the Jet Propulsion Laboratory, California Institute of Technology, under contract with the NASA.

REFERENCES

Booth R. S., de Block W. J. G., Jonas J. L., Fanaroff B., 2009, preprint (arXiv e-prints, 0910.2935)
Browne I. W. A., Savage A., Bolton J. G., 1975, MNRAS, 173, 87P
Carilli C. L., Rawlings S., 2004, New Astron. Rev., 48, 979
Collioud A., Charlot P., 2009, in Bourda G., Charlot P., Collioud A., eds, 19th European VLBI Geodesy Astrometry Working Meeting. Université Bordeaux 1-CNRS, p. 19
Denicoló G., Terlevich R., Forbes D. A., Terlevich A., Carrasco L., 2005, MNRAS, 356, 1440
di Serego-Alighieri S., Danziger I. J., Morghanti R., Tadhunter C. N., 1994, MNRAS, 269, 998
Fey A. L., Charlot P., 1997, ApJS, 111, 95
Fey A. L., Charlot P., 2000, ApJS, 128, 17
Fey A. L., Clegg A. W., Fomalont E. B., 1996, ApJS, 105, 299
Fey A. L. et al., 2004a, AJ, 127, 1791
Fey A. L., Ojha R., Reynolds J. E., Ellingsen S. P., McCulloch P. M., Jauncey D. L., Johnston K. J., 2004b, AJ, 128, 2593
Fey A. L. et al., 2006, AJ, 132, 1994
Fey A. L., Gordon D., Jacobs S., 2009, IERS Technical Note, 35, 204, ISBN 3-89888-918-6
Greisen E. W., 1998, Albrecht R., Hook R. N., Bushouse H. A., eds, ASP Conf. Ser. Vol. 145, Astronomical Data Analysis Software and Systems VII. Astron. Soc. Pac., San Francisco, p. 204
Halpern J. P., Eracleous M., Mattox J. R., 2003, AJ, 125, 572
Hewitt A., Burbidge G., 1989, ApJS, 69, 1
Jauncey D. L., Batty M. J., Gulkis S., Savage A., 1982, AJ, 87, 763
Jauncey D. L., Batty M. J., Wright A. E., Peterson B. A., Savage A., 1984, ApJ, 286, 498
Johnston S. et al., 2008, Exp. Astron., 22, 151
Jones D. H. et al., 2005, Publ. Astron. Soc. Aust., 22, 277
Jones D. H. et al., 2009, MNRAS, 399, 683
Linfield R. P. et al., 1989, ApJ, 336, 1105
Marziani P., Sulentic J. W., Dultzin-Hacyan D., Calvani M., Moles M., 1996, ApJS, 104, 37
Ojha R. et al., 2004a, AJ, 127, 3609
Ojha R., Fey A. L., Jauncey D. L., Lovell J. E., Johnston K. J., 2004b, ApJ, 614, 607
Ojha R. et al., 2005, AJ, 130, 2529
Osmer P. S., Porter A. C., Green R. F., 1994, ApJ, 436, 678
Peterson B. A., Jauncey D. L., Condon J. J., Wright A. E., 1976, ApJ, 207, L5
Piner B. G., Mahmud M., Fey A. L., Gospodinova K., 2007, AJ, 133, 2357
Rees M. J., 1997, Rev. Modern Astron., 10, 179
Schilizzi R. T. et al., 2007, SKA Memo, 100, 53
Shepherd M. C., Pearson T. J., Taylor G. B., 1995, BAAS, 27, 903
Stickel M., Fried J. W., Kuehr H., 1989, A&AS, 80, 103
Stickel M., Kuehr H., Fried J. W., 1993, A&AS, 97, 483
Strittmatter P. A., Carswell R. F., Gilbert G., Burbidge E. M., 1974, ApJ, 190, 509
White G. L., Jauncey D. L., Wright A. E., Batty M. J., Savage A., Peterson B. A., Gulkis S., 1988, ApJ, 327, 561
Wilkes B. J., 1986, MNRAS, 218, 331
Wills D., Lynds R., 1978, ApJS, 36, 317
Wright A. E., Peterson B. A., Jauncey D. L., Condon J. J., 1979, ApJ, 229, 73
Zensus J. A., Ros E., Kellerman K. I., Cohen M. H., Vermeulen R. C., Kadler M., 2002, AJ, 124, 662

SUPPORTING INFORMATION

Additional Supporting Information may be found in the online version of this article:

Figure 2. Images of the 31 sources in our sample.

Please note: Wiley-Blackwell are not responsible for the content or functionality of any supporting materials supplied by the authors. Any queries (other than missing material) should be directed to the corresponding author for the article.

This paper has been typeset from a TEX/LATEX file prepared by the author.